CITY UNIVERSITY OF HONG KONG

Development of a Smart Wireless Charging System for Robotics

Submitted to
School of Energy and Environment
in Partial Fulfilment of the Requirements
for the Degree of Bachelor of Engineering in
Energy Science and Engineering

by

SHARMA Milind

2023.4

2

s

<u>Outline</u>

Acknowledgements:

I would also like to express my gratitude to my FYP supervisor, Dr. Chunhua Liu, for his invaluable guidance, suggestions, and unwavering support throughout the entire duration of this project. His expertise and advice have greatly contributed to my academic growth and the development of my research and writing skills. Additionally, I would like to extend my sincere appreciation to my mentor, PhD candidate Yuxin Liu, who has been instrumental in shaping my research direction, expanding my professional knowledge, and honing my practical skills.

Wireless power transfer was initially an unfamiliar area for me, and I encountered numerous unforeseen challenges while commissioning my prototype. With the continuous support and encouragement from my mentor, supervisor, and the grants and projects mentioned above, I was able to overcome these obstacles and successfully complete my project. Their combined expertise and backing have been indispensable in my journey, and I am extremely thankful for their mentorship and assistance.

Abstract:

This paper presents the development of a smart wireless charging system for robotics, focusing on the integration of IoT technology and an LCC-S compensation-based one-to-one system operating at 100 kHz. The primary goal of this research is to provide a smart, remote-controlled, and monitored wireless power transfer (WPT) system that is tailored to charging robotics systems. By integrating IoT technology, the system allows users to remotely control and monitor the WPT system via a dashboard, which displays crucial information such as charging voltage, current, output power, efficiency, and the presence of a secondary coil. Furthermore, the dashboard facilitates the remote control of the charger's on/off state. In addition to remote control and monitoring, the IoT system enables feedback control for the primary side, switching between active and standby modes based on the detection of the secondary coil. In active mode, the inverter provides constant output to the transmitter coil, while in standby mode, the output pulses every 500 ms to conserve energy. The IoT system also dynamically adjusts the phase-shift control in the inverter to regulate output power on the secondary side, meeting target power requirements. The proposed WPT system demonstrates a maximum efficiency of 64.28% with a power transfer of 75 W across a 4 cm air gap, with potential for higher power transfer untested due to equipment limitations. While designed for the Hunter SE rover, the system can be easily adapted for use with other robotic platforms. This smart wireless charging system offers significant improvements over existing solutions, including real-time remote control and monitoring, seamless IoT integration, adaptability to various robot models, and enhanced charging efficiency.

Chapter 1: Introduction:

1.1.   Research Background:

The advent of the electrical age has led to extensive discussions and research on charging and power transformation technologies. Traditional charging methods that rely on wired connections, provide considerable power capacity and efficiency but limit mobility, reduce durability and aesthetics, and impede waterproofing capabilities. Nikola Tesla revolutionized the concept of wireless power transfer (WPT) with the invention of the Tesla Coil, a high-frequency, air-core, resonant transformer capable of generating very high voltages and creating electrical discharges. The Tesla Coil was designed to transmit electrical energy wirelessly through the Earth's atmosphere, and established the foundation for further research into WPT technologies [1]. Near-field non-radiative transfer emerged from this area, which enabled wireless energy transfer across short distances but with relatively low power outputs.

A pioneering study conducted by a team at MIT in 2007, as illustrated in Figure 2, introduced magnetic resonance power transfer (MRPT), allowing electricity to be transmitted through an air gap over a few metres with high power capacity [2]–[4]. Innovations like this provided WPT with the credibility and practicality needed to gain broader adoption and commercial success, as evidenced by products from WiTricity Corporation [5]. Today, advances in WPT technology, combined with 'smart' technology, have led to the integration of smart wireless chargers in most mainstream devices, such as mobile phones, laptops, and headphones. These chargers typically feature overcharge protection, automatic shut-off when the device is fully charged, LED indicators for charging status, adjustable charging speeds based on battery health, and charge optimization, ultimately aiming to deliver efficient charging alongside an excellent user experience.

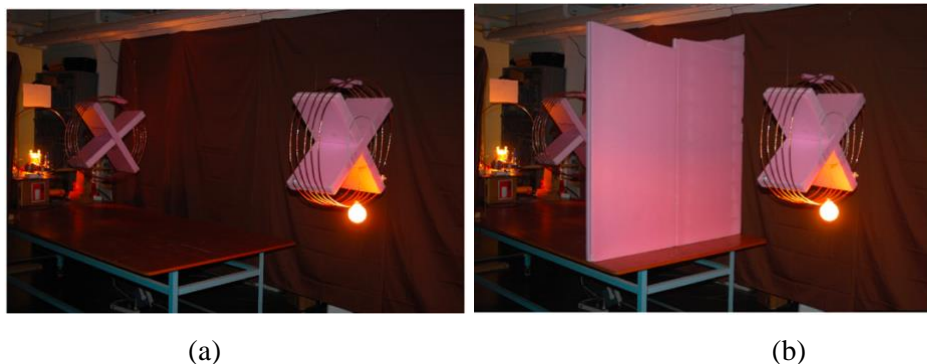(a)   (b)
Figure 1: WPT 60W light bulb over 2m distance. (a) Without barrier. (b) With barrier. [2]

The field of robotics, however, has been slow to adopt and implement this technology. Previous studies on the integration of smart WPT systems with robotics have focused mostly on coil topologies [6], multiple device charging [7], [8], efficient charging algorithms [9], and better compensation networks [10]. While these are important areas of research to continue the improvement of the underlying WPT technology, these papers do not provide a framework to create charging systems that are easy and modern to control and monitor – both of which are core tenets of smart technology. Therefore, there is a need for a solution that integrates true smart features with effective wireless charging abilities and a simple system architecture.

1.2.   *Research Objectives:*

The main objective of this project is to build a wireless charging system for a specific robot platform, with a novel solution to provide misalignment tolerance, as well as a smart dashboard and user control interface.

The tasks performed in order to accomplish this goal are listed below:

1. Literature review of the background and history of wireless power transfer, with a focus on the employment of smart technology in this field.
2. Overview of the design of the WPT system built.
3. Summary of different coil topologies, as well as a detailed analysis on the single primary, single secondary coil system selected for this project.
4. Design and fabrication of a custom high power inverter circuit board.
5. Analysis of compensation network options, as well as justification and explanation of the LCC network selected for this project.
6. Integration of a smart online dashboard for control and monitoring of charging system using Internet of Things (IoT) technology.

Chapter 2: Literature Review:

Large amounts of research have been done on the field of wireless power transfer and wireless charging. This section contains a thematically organised summary of the knowledge required to build an intelligent wireless charging system for a robotics platform.

2.1.   Development of Wireless Power Transfer:

Conventional charging systems involve connecting a charging plug to a device for power transfer. This method has several disadvantages: the wire and plug may deteriorate due to constant plugging and unplugging; the device is confined to a specific location; and sparks may be produced. Over the years, a wire-free charging technique known as wireless power transfer has emerged, eliminating the constraints associated with wired charging. This technology has become increasingly popular and now has numerous applications, including smartphone and headphone charging [11], implantable medical devices [12], electric vehicle wireless charging [13], and drone and logistics robot charging [14], [15].

In 1888, Heinrich Hertz discovered the existence of electromagnetic waves and conducted research into their behaviour. His work helped future scientists understand the concepts of electromagnetic waves, laying the foundation for future research into this field [16]. Nikola Tesla, in 1891, made many important contributions to the field of WPT, such as the aforementioned Tesla coil [1]. However, following this period, due to constraints in electronic components and related technology, there was limited product development and research during the early 20th century. Over the following decades, the popularity of radiation-based WPT gradually increased and in 1966, American engineer William C. Brown conducted a point-to-point power transfer experiment using radiation, achieving an efficiency of 26% [17]. Subsequently, in 1968, scientist Peter Glaser theorised about a large solar powered satellite system capable of converting solar radiation into electromagnetic beams and transmitting solar energy to Earth [18].These developments eventually led to the popularisation of non-radiative near-field WPT, which can be further divided into inductive coupling and magnetic resonant coupling WPT, also known as resonant inductive coupling. Simple inductive coupling relies on the concept of induced EMF to transfer energy across an air gap. Magnetic resonant coupling improves on this by additionally also setting both coils to the same resonant frequency, greatly increasing efficiency and range. The operating frequencies and transmission ranges of different WPT systems can be seen in figure 2.
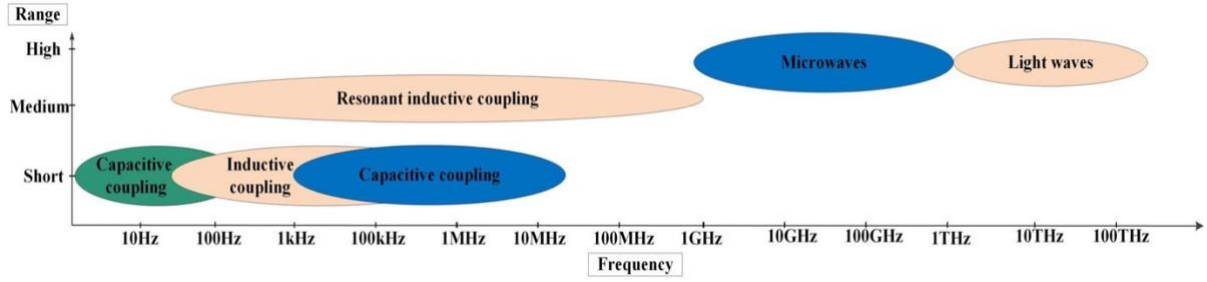
Figure 2: Review of different technologies in WPT [13].

2.2. *Fundamental Concepts of Wireless Power Transfer:*

Wireless power transfer (WPT) is broadly governed by two fundamental laws of physics, Ampere's Circuital Law and Faraday's Law of Induction. Ampere's Law states that when a current flows through a conductor, a magnetic field is generated whose strength is proportional to the magnitude of the current and the permeability of free space [19]. This relationship can be mathematically expressed as follows:

$$\oint \vec{B} \cdot \vec{dl} = \mu_0 NI \tag{1}$$

Faraday's Law of Induction, on the other hand, states that a time-varying magnetic flux intersecting a surface formed by a conducting coil induces a time-varying electromotive force in the circuit, whose magnitude is proportional to the rate of change of the flux and the number of turns in the coil [20]. This induced emf creates induced current. Mathematically, this is expressed as follows:

$$induced\ emf = -N \cdot \frac{d\phi}{dt} \tag{2}$$

Together, these laws provide a fundamental model for the interaction between electric currents, voltages, and magnetic flux in WPT systems. In such systems, two coils, primary and secondary, are separated by an air gap, and high-frequency alternating current is passed through the primary coil. This creates a time-varying magnetic field around it, as described by Ampere's Law. Part of this magnetic flux intersects with the surface formed by the secondary coil. The amount of flux that interests with the secondary coil is directly related to the coefficient of coupling, k, with higher coupling implying higher efficiency. In accordance with Faraday's Law, the magnetic flux induces an emf in the secondary coil, which produces a current.

However, such systems are inductive but non-resonant and suffer from significant energy losses through leakage inductance and copper losses in the coils. Coupling efficiency decreases as the distance between coils increases, making them suitable mostly for close-range power transfer. For mid-range WPT, an inverter with a large V-A rating would be required to transmit sufficient power [13]. To fix the flaws of simple inductive coupling, magnetic resonant coupling is introduced in most practical modern systems. It is well known that two resonant objects are highly efficient at exchanging energy, while nearby non-resonant objects are largely ignored. Therefore, the suitability of magnetic resonance for WPT is even higher since most everyday objects do not interact with magnetic fields [13].
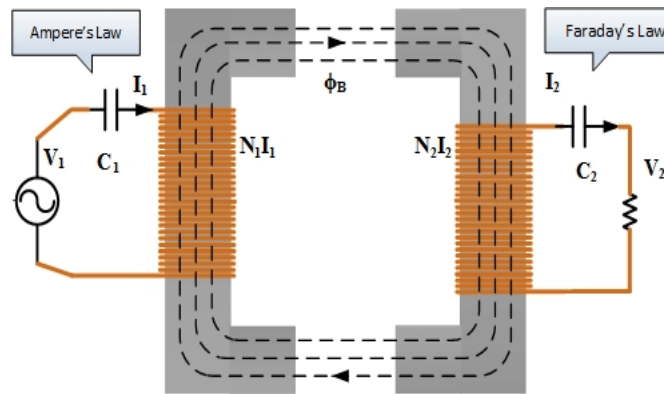
Figure 3: Fundamental concepts of WPT [13].

2.3.   *Integration of Smart Technology with Wireless Power Transfer:*

Smart technology, also referred to as the Internet of Things (IoT), consists of a wide array of interconnected devices leverage advanced sensors, data processing, and communication capabilities to form a system that can perform tasks intelligently and autonomously [21]. This technology can be used to develop solutions that enhance efficiency and user experience by providing a constant stream of information about all devices of any kind in the network [22]. The feature that is key to the effectiveness of smart technology is the ability to process and analyse real-time data. If applied to a WPT system, this technology could be used to communicate between the transmitter and receiver coils, provide real-time charging related information to the user, and even detect issues such as coil misalignment in the charging process.

In [23], a smart, autonomous WPT system is proposed to enable easy charging for electric wheelchairs. The paper presents a supervisor system which continuously coordinates and analyses data between the charging dock and the wheelchair receiver coil, thus maintaining

safe operation of the charger at a high level, without requiring human interference. A similar approach to create a smart wireless charging system for electric wheelchairs is described in [24], using technology closer to modern IoT to create a hands-free system that communicates with the central computer of the system via Robot Operating System (ROS) and provides an Android app that displays charging information and allows the user to control the power transmitter.

There have also been other approaches to make wireless charging systems more modern, capable, and intelligent, which can be somewhat classified as smart WPT. One main approach to improving wireless charger capabilities is through the exploration of multiple-transmitter/receiver coil configurations. Multiple transmitter coil systems have been used for the purpose of Dynamic Wireless Power Transfer (DWPT). This variation of WPT technology aims to enable charging of robots while they operate and are in motion, which is an improvement over static charging, and could be considered smart charging. One analysis designed a DWPT system for logistics robots, such as the ones used in warehouses [15]. This system utilises a many-to-one coil arrangement and an LCC-S compensation network to enable dynamic charging, and was able to achieve a maximum efficiency of 74.51% at 1.5 kW rated power with the receiver in motion. Other studies have looked into multicoil transmitter arrays as a method of achieving more intelligent charging. In such systems, misalignment tolerance is addressed by tracking the position of the receiver coil through detecting changes in transmitter coil characteristics, and only using aligned coils to transmit power to the receiver [6].

'Smart' multiple receiver coil systems (one-to-many) have also been explored. One such system, designed with a single transmitter and 3 miniature receiver coils, developed a method based on separating the resonant frequencies of the receivers to select and deliver power to only one receiver coil at a time, eliminating cross coupling losses [25]. Using this approach, a maximum efficiency of 29% was observed despite the small coupling coefficient of only 0.01. These advanced coil arrangements each have specialised advantages. One-to-many chargers allow for charging of multiple devices; many-to-one arrangements provide much greater misalignment tolerance; many-to-many arrangements incorporate advantages of both. While these different coil arrangements are often necessary to solve certain problems, they do not make use of the advancements of the IoT sector. Thus, they forego the benefits of online monitoring, remote control, and more advanced communication channels.

Another area of advancement for wireless charging has been in the development of charging standards, such as the "Qi Standard" developed by the Wireless Power Consortium and "Power Matters Alliance Standard" (PMA) developed by the Airfuel Alliance. Among other things, these standards specify the design of a communication standard between the transmitter and receiver [11]. This is related to smart technology as it provides the simplicity to use any standard-compliant transmitter-receiver pair and have the wireless charging work correctly. It is important to note that transmitter-receiver communication occurs over the same coils used for charging, adding a degree of complexity to the charger design [26]. The PMA standard does incorporate smart features, emphasizing cloud-based device management, offering smart features such as usage monitoring, remote diagnostics, and over-the-air firmware updates [11].

(a)   (b)
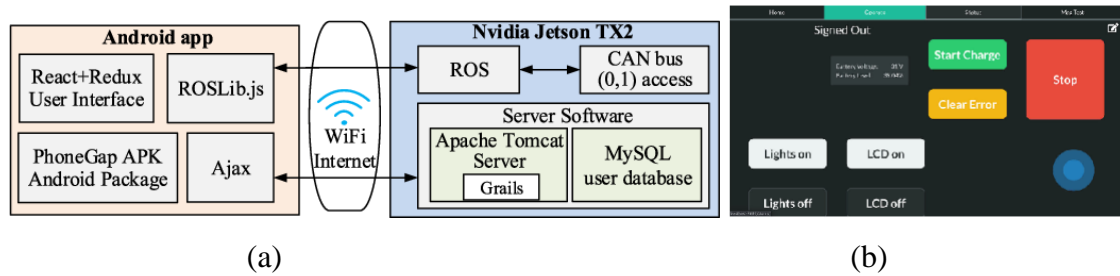
Figure 4: Smart interface for WPT system [24]. (a) Relationship between system central computer and android app. (b) Android mobile application used for monitoring and control.

(a)   (b)
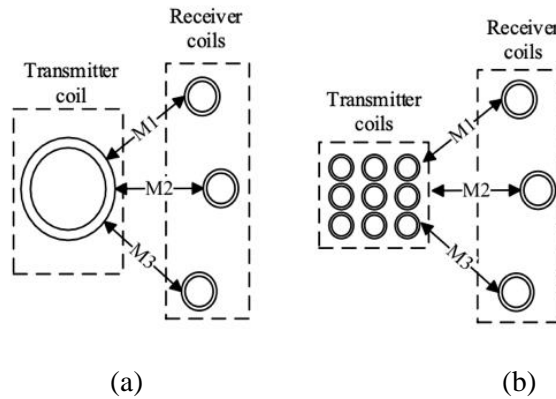
Figure 5: Multiple receiver coil topologies; (a) Single In Multiple Out (SIMO) and (b) Multiple In Multiple Out (MIMO).

2.4.   *Motivation and Description of the Project:*

The motivation for pursuing this project comes from my experience in robotics and software development. During a summer internship at a robotics company, I noticed that in most cases, the robots had to be manually charged using a wired connection – a repetitive task that should have been rendered outdated with the popularisation of wireless charging and smart

technology. Further research revealed that most robotics systems that are WPT enabled are either very high power applications (kW), very low power application of a few Watts or less [27]. As such there is a dearth of ready-made medium power WPT capabilities for robotics platforms.

The purpose of this project is to introduce a truly smart wireless power transfer system that is custom built for a specific robotics system, to provide exact charging voltage and current that it requires. Affordable and modern IoT technology connected to the WPT system will enable the creation of a multi-platform, online charger control and monitoring dashboard. Information gathered by the IoT devices on the receiver and transmitter sides will also be analysed in order to implement a feedback and control system. Using this, the transmitter coil will be switched to standby mode if receiver coil is not detected to save energy. Also the inverter output power will be varied using phase-shift control, based on the feedback obtained from the secondary coil. The system will use an internet enabled microcontroller board on both the transmitter and receiver sides in conjunction with other system elements to facilitate the IoT features. The proposed system will feature a one-to-one (O2O) coil arrangement where both coils are identical in size and shape to simplify the coil architecture. An appropriate LCC compensation network will utilised in order to reduce sensitivity to variations in coupling coefficient and load impedance, which leads to higher stability and efficiency. The online dashboard will be used to control the charger system and view charging information in real-time remotely. This, along with a modern and appealing design for 3D printed enclosures will result in a WPT system that is both a capable charger and also user friendly and visually appealing.

Chapter 3: Methodology:

The section on methodology consists of two sections. The first section, theoretical framework, contains all the theoretical concepts and design principles involved in this project. The second section, experimental methodology, covers the steps taken for the practical design of the system, how certain parameters were experimentally determined, and how certain components were selected. This includes measurements, simulations, and other practical design decisions.

3.1. Theoretical Framework:

3.1.1. General System Architecture:

Figure 7 displays the architecture of the smart WPT system proposed in this paper. In this section, a general system overview is provided with a focus on the WPT parts, while section 3.1.6 covers the IoT network structure in detail.

On the primary side, stable DC power is supplied to the inverter, which then modulates it into a modified square wave. The transmitter (Tx) coil is energised by the modified square wave and compensated by the LCC network so it resonates at the system operational frequency. In this state, the Tx coil transfers energy to the receiver (Rx) coil across an air gap. On the secondary side, the induced voltage produces alternating current, which is then compensated and rectified into direct current. The direct is then used to charge the load. The proposed coil design consists of inverter, LCC-S compensation network, and one-to-one transmitter and receiver coil system. The primary and secondary side are both additionally monitored by internet enabled microcontrollers, which process and send charging information to an online database. This information is then available for viewing on the online dashboard, and also used to implement feedback control for the primary side without manual operation.
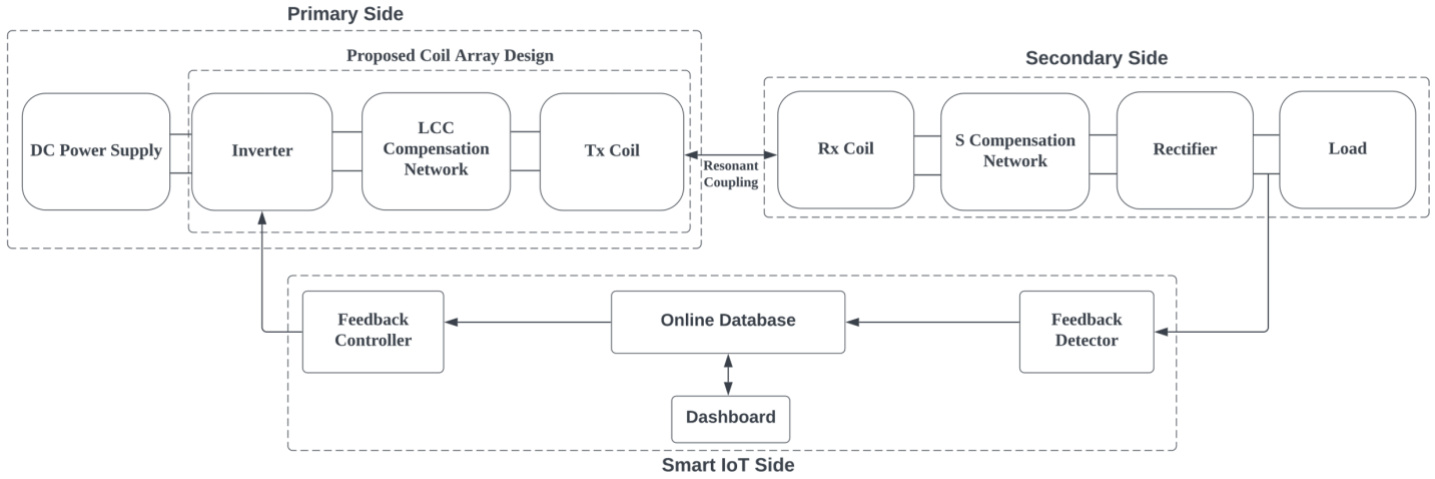
Figure 6: System architecture of proposed smart WPT system

3.1.2. *Coil Topology:*

In this paper, a one-to-one coil (O2O) topology – as shown in figure 8 [28] is proposed, utilizing identical circular coils for both the primary (transmitter) and secondary (receiver) sides. This configuration provides a simple approach to wirelessly transfer power between the charging station and the robot, which reduces system complexity.

A O2O topology is a suitable choice for applications where a single transmitter coil (TX) is supposed to charge a single receiver coil (RX) on the robot. This configuration offers the advantage of straightforward design, as it does not require the complex control mechanisms and communication protocols needed for multi-coil arrangements. O2O coil topologies also simplify the problem of stable and efficient power transfer in the event of misalignments between the charging station and the robot, as fewer coil positions have to be taken into account. Lastly, the simple design of the O2O topology allows this paper to focus on the implementation of a robust smart IoT network.
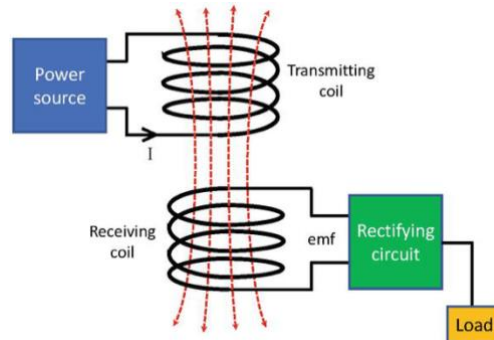

Figure 7: One-to-one coil topology [28].

3.1.3. *Coil Modelling:*

Prior to design of the physical coils, coil modelling was performed to obtain estimations of their properties in advance. As described in detail in section 3.2.2., circular coils were chosen for this system. These parameters were modelled for circular coils: self-inductance; inner diameter; coil area. All modelling in this section is based on the framework laid out in [29] as applied in [30], and can calculate inductance with ~1% maximum error:

$$D_{in}(mm) = D_{out} - (2N \cdot (d_{wire} + s)) \tag{3}$$

Where D_{in} is inner diameter of coil, D_{out} is outer diameter of coil, N is number of turns, d_{wire} is wire diameter, s is turn spacing (all distances are in mm). Wire length can be calculated from this as well, which can help derive coil resistance.

$$wire\ length\ (m) = \frac{N\pi}{1000} \cdot \frac{(D_{in} + D_{out})}{2} \tag{4}$$

Inductance can also be estimated in this manner. R and W are intermediate parameters used for this calculation, and their derivations are in the Appendix.

$$inductance\ (\mu H) = \frac{R^2 \cdot N^2}{8R + 11W} \tag{5}$$

3.1.4. *LCC-S Compensation Network:*

For the system proposed in this paper, a LCC-S (inductor-capacitor-capacitor-series) compensation network is utilised. The decision to utilise an LCC network is based on the principle that it can facilitate constant output voltage and constant primary coil current. The working principles behind this compensation technique are discussed in this section.

The requirement for a compensation network in WPT systems stems from desire to improving certain characteristics in the system. For the system proposed in this paper, those characteristics include: constant current/constant voltage output that is not sensitive to load resistance; Low input reactive power, Low sensitivity to variation in the coupling coefficient, which can broaden the range of possible applications [31]. Of the many initial compensation networks that emerged as options, series-series (SS) compensation was the most effective to achieve these goals [32]. However, due to low performance in the event of coil misalignment, higher order compensation such as LCC networks have been explored [33], [34]. Figure 8

shows the practical configuration of the LCC-S compensation network, where L_{P1}, C_{P1} and C_{P2} are the inductance, parallel capacitance, and series capacitance in the compensation network, and L_P is the inductance of the primary coil. As mentioned earlier, a feature of LCC compensation networks is that when operating at the resonant frequency, transmitter coil current is independent of the coupling coefficient and secondary coil load, facilitating constant current output for the transmitter. In order for this to happen, the following relationships must be satisfied [33]:

$$j\omega L_{P1} = -\frac{1}{j\omega C_{P1}} \rightarrow L_{P1} \cdot C_{P1} = \frac{1}{\omega^2} \tag{6}$$

$$j\omega L_{P1} = j\omega L_P + \frac{1}{j\omega C_{P2}} \rightarrow (L_{P1} \cdot L_P) \cdot C_{P2} = \frac{1}{\omega^2} \tag{7}$$

To further analyse the LCC compensation, Figure 9 shows the T-equivalent circuit diagram of the resulting system when the transmitter and receiver coils are coupled together, which is used for showing the constant primary current. The impedance reflected from the secondary side is represented here as Z_{re1}. Using this, the total impedance on the primary side can be calculated:

$$Z_0 = j\omega L_{P1} + \frac{1}{j\omega C_{P1}} \,||\, \left(\frac{1}{j\omega C_{P2}} + j\omega L_P + Z_{re1}\right) \tag{8}$$

Simplifying (8) using equation (6) and (7), we derive a new equation for Z_0:

$$Z_0 = \frac{\omega^2 \cdot L_{P1}{}^2}{Z_{re1}} \tag{9}$$

This can now be used to model the current in the transmitter coil, assuming that the voltage provided in the transmitter coil by the inverter is U_{in1}. Equation (5) can be then be derived:

$$I_{P1} = \frac{U_{in1} \cdot \frac{1}{j\omega C_{P1}} \,||\, \left(\frac{1}{j\omega C_{P2}} + j\omega L_P + Z_{re1}\right)}{Z_0 \cdot \left(\frac{1}{j\omega C_{P2}} + j\omega L_P + Z_{re1}\right)} \tag{10}$$

Which can then be simplified further to:

$$I_{P1} = \frac{U_{in1}}{j\omega L_{P1}} \tag{11}$$

Equation (11) shows that the value of I_{P1}, the transmitter coil current, is not dependant on the impedance reflected from the secondary side. This ensures that any variation in mutual inductance that occurs when the robot is moving on the charging station does not affect the current in the primary coil.
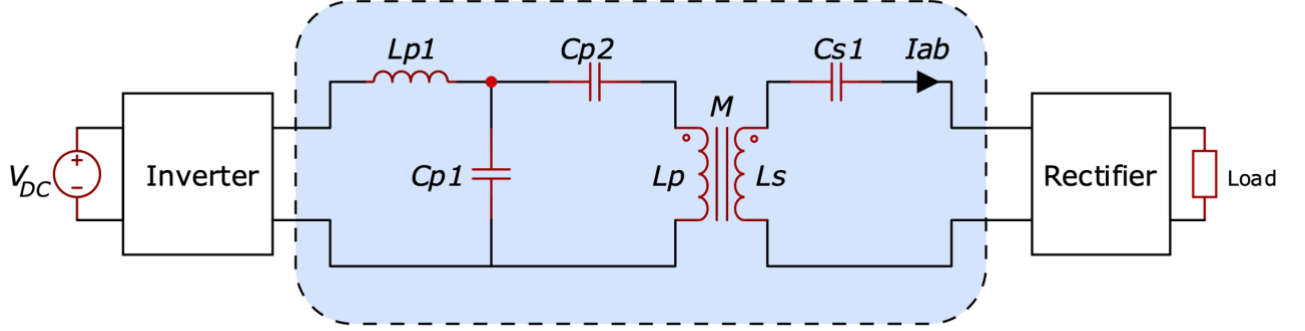

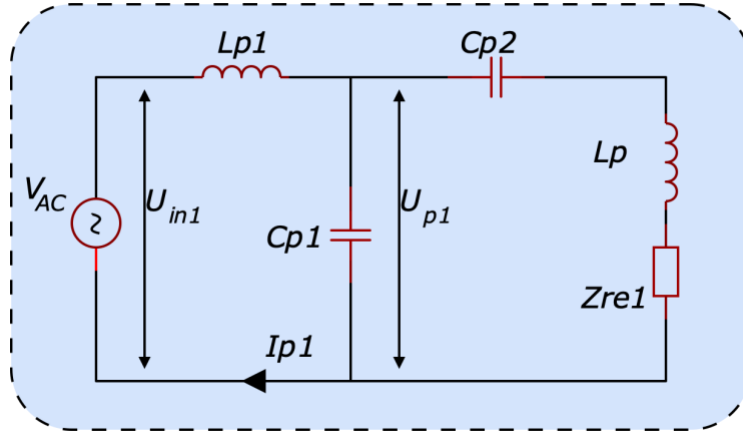Figure 8: Practical configuration of LCC-S Compensation Network.

Figure 9: T-Equivalent circuit of primary side to show constant Tx coil current.

3.1.5. *Inverter Control Algorithm:*

For this system, phase-shifted pulse width modulation (PWM) with dead-time insertion is used to control the inverter [35]. An H-Bridge circuit can be driven by 4 PWM signals to control the voltage waveform on the primary of a transformer, or in the case of this paper, a WPT system. The PWM signals are generated as two pairs of complementary signals, with one pair phase shifted by an angle of θ in comparison with the other. As a result, the primary coil receives the bottom waveform – known as a modified square wave - across its terminals. The RMS voltage of this waveform is directly controlled by the degree of phase shift between the two sets of square waves. A phase shift of $\theta = 0°$ results in minimum voltage output, while a phase shift of $\theta = 180°$ results in maximum voltage output. Independent of the phase

shift, no DC component appears in the load voltage provided the square wave duty cycle remains at 50%. This is well suited for inductive loads, and as a result, this is frequently used in WPT system inverters to deliver an adjustable amount of power to the Tx coil [36]. Figure 10 shows the four PWM signals, as well as the 90° phase shift that will be used as standard operation, although the amount of phase shift will be dynamically adjusted during the operation of the system. Dead-time is also added in between complementary signal edges. This is a short period where both MOSFETs in the same leg of the H-bridge are signalled to switch off, to prevent a short circuit, or 'shoot-through' from occurring.

This phase-shift output can be easily implemented in a 32 bit microcontroller board, such as the i.MX RT1060, reducing cost and complexity. The choice of microcontroller board is discussed in detail in 3.2.9.
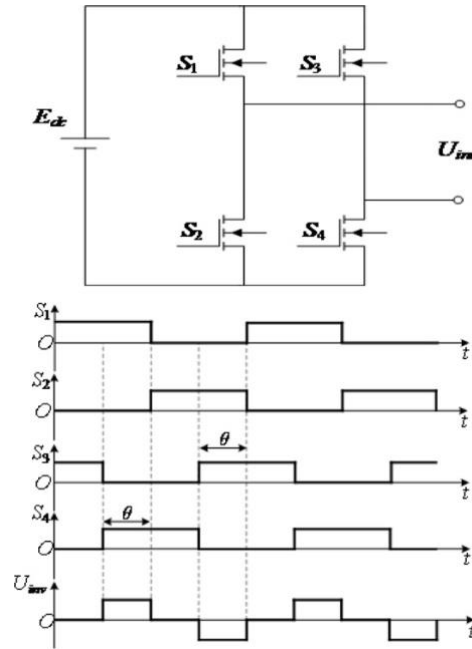
Figure 10: H-bridge configuration with phase shifted PWM control signals, with modified square wave output [38].

3.1.6. *IoT Network Structure:*

A smart IoT network, as shown in figure 11, is integrated with the WPT system in this paper. This network consists of four main blocks: The secondary side feedback detector; Primary side feedback controller; Online database; and Control and monitoring dashboard. An explanation of how all system blocks interact with each other is provided below.

Moving from the right to the left, the secondary side feedback detector block is responsible for detecting the DC voltage and current being supplied to the load by the rectifier. It uploads this data to the database in real-time, from where it can be viewed on the online dashboard. The information is also constantly synchronised to the primary side feedback controller, which then tells the inverter whether to increase or decrease the voltage in the Tx coil.

Additionally, the AC voltage and current in the Tx coil is also measured by sensors, and synchronised to the database in real-time. This allows for live measurement of power transfer efficiency, $\eta = \frac{V_S \cdot I_S}{V_P \cdot I_P}$, which can also be displayed on the dashboard for the user to view. Lastly, the entire system can be switched between modes such as on/off/standby remotely from the control dashboard. An explanation of the effect of these modes is provided in 3.1.7.
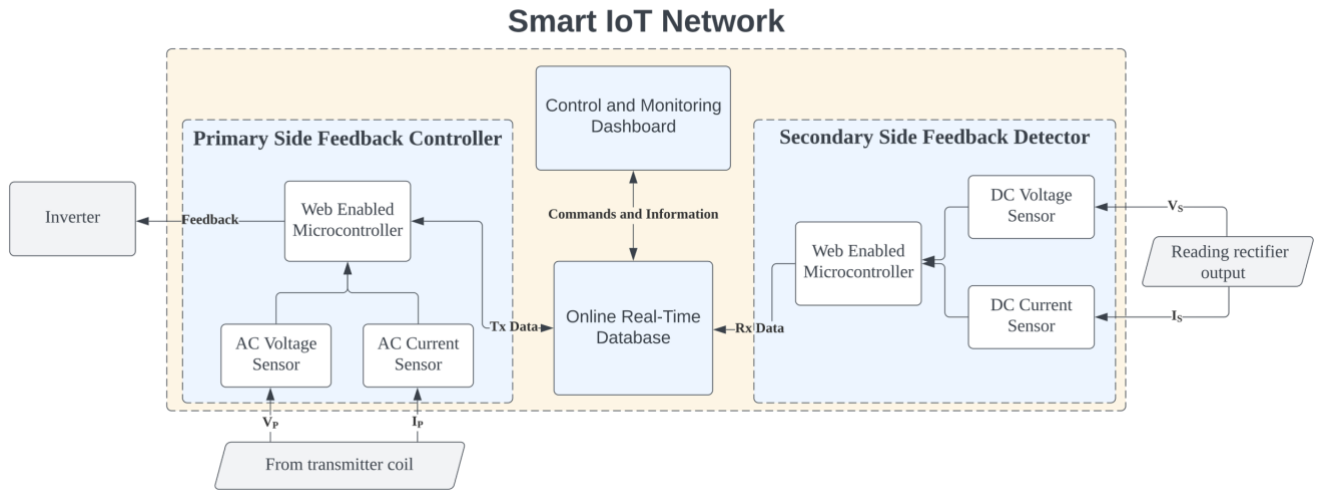

Figure 11: Smart IoT network for WPT system.

3.1.7. *Smart Feedback Control Algorithm:*

Figure 12 shows the closed-loop algorithm that controls the flow of the sensing of Rx side voltage and current, and the signal sent to the inverter. Voltage and current induced in the Rx coil will rise as the coil approaches the Tx coil, and in this way the presence of the Rx coil can be detected, and feedback control for the inverter can also be implemented.

The modes work in the following manner: The inverter can be OFF, STANDBY, and ACTIVE modes. When the inverter receives a disable command, it's in OFF mode, where there is no output. If the inverter receives an enable command but the Rx coil is not detected, the inverter is placed in STANDBY mode, where it pulses voltage in the Tx coil only

periodically. As the secondary side voltage is continuously sampled, this is used to check the presence of the Rx coil on the charging pad – If this voltage crosses a threshold, the Rx coil is considered detected and present on the charging station. The inverter then is placed in ACTIVE mode, where it continuously generates the output waveform to power the Tx coil. This is shown clearly in table 1.

The feedback control works in the following way. When the inverter is in ACTIVE mode, but the secondary voltage is still insufficient to charge the robot battery, then the inverter is signalled to increase the degree of phase shift to increase the voltage. It should be noted that there is a limit to the voltage that the inverter can produce in this manner, but it would still increase the overall tolerance to misalignment greatly.

Table 1: State table for mode control.

Enable command received?	Rx coil detected?	Mode
No	N/A	OFF
Yes	No	STANDBY
Yes	Yes	ACTIVE
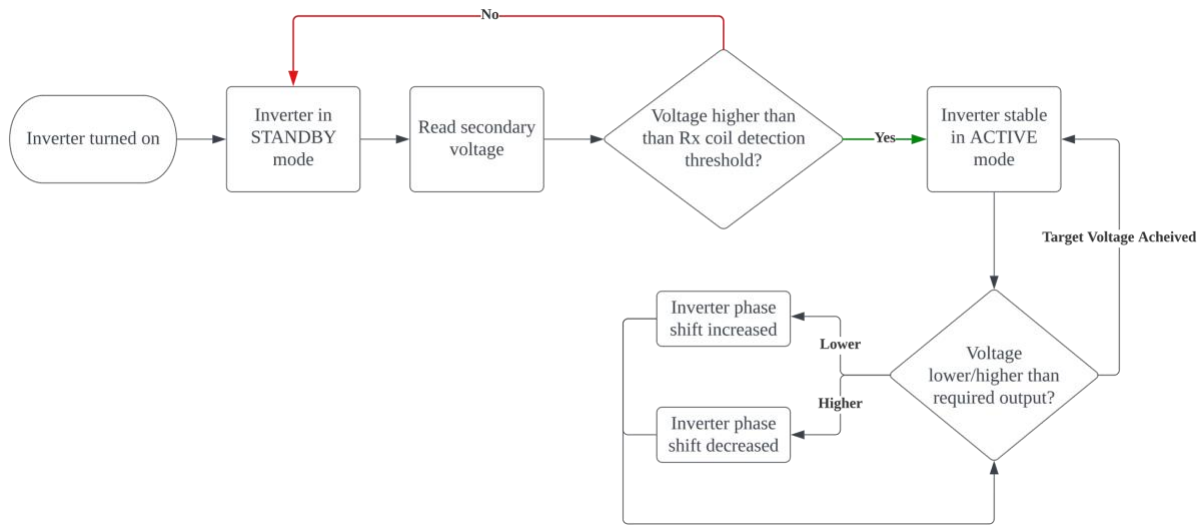
Figure 12: Closed loop algorithm to implement smart feedback.

3.2. *Experimental and Practical Setup:*

3.2.1. *Selection of Robot Platform:*

For the practical implementation of the smart WPT system described in this paper, a robotics platform had to be selected. I was given the choice between two robots that were available in the laboratory at the time. Figure 14 (a) shows the first option - Xiaomi's CyberDog Bionic

Quadruped robot, while figure 14 (b) shows the second option – the Hunter SE rover by AgileX.

The Hunter SE Rover was chosen as the robotics platform for this project for two reasons:

1. Level Underside: For this WPT system, the Rx coil has to be mounted on the underside of the robot chassis. In the case of the quadruped robot, the relative angle of the chassis changes with respect to the ground, where the charging station would be placed. This would add complexity and require greater amounts of misalignment tolerance that go beyond the scope of this project. As such as the flat, constantly level chassis of the rover provides the perfect mounting point for the Rx coil and secondary circuit components.

2. Lower Dynamic Stress: The Rx coil, rectifier, and secondary side IoT components would all be mounted to the robot. For quadruped robots, due to their jerky movements while walking, there would be higher dynamic stress on these components. Once again, this would add complexity to a project where the focus is the development of a smart WPT system. Instead the smooth movement of the rover provided a better development platform for this purpose.

(a)   (b)

Figure 13: Robotics platform options. (a) CyberDog Bionic Quadruped Robot [37]. (b) Hunter SE Rover [38].

3.2.2. *Charger Output Requirements:*

The Hunter SE Rover has the following charging requirements [39]:

Charging voltage: 24V DC (constant voltage)

Charging current: 15A maximum current.

3.2.3. _Coil Design:_

Designing optimal Rx and Tx coils is essential for any WPT system. For this project, I started the process of coil design by looking at the initial constraints. Since the Rx coil must be mounted on the underside of the Hunter SE rover chassis, one important constraint is the size and shape of this coil. I aimed to use the largest coil size possible for the Rx/Tx coils, as this allows for greatest power transfer. Figure 15 shows the dimensions of the robot, from which it is clearly visible that the width of the robot, equal to 230 mm, would be the limiting factor [38]. I also physically verified this measurement.

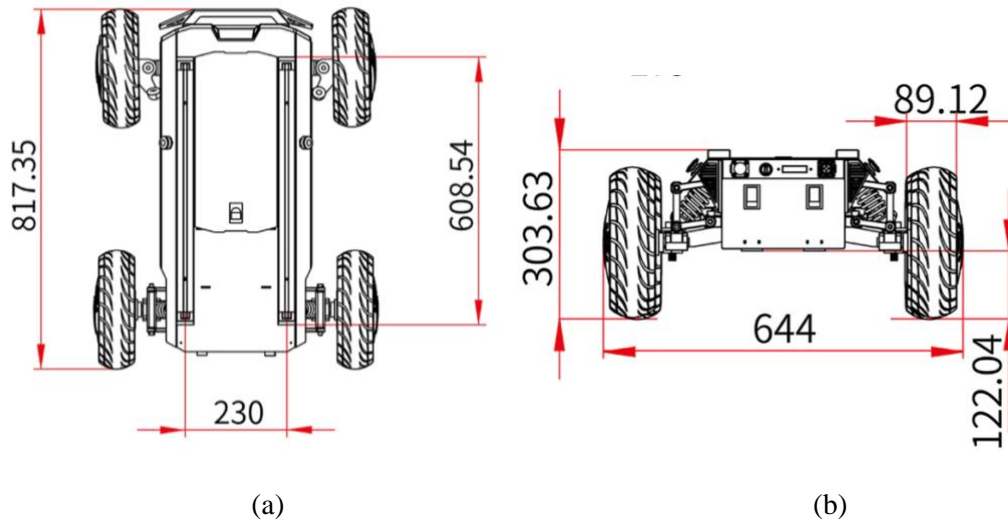(a)   (b)

Figure 14: Dimensions of the Hunter SE rover (a) Top view. (b) Front view [38].

I chose to use circular coil (planar spiral) for the Tx/Rx coils, due to the following reasons:

1. Symmetric magnetic field distribution, providing intrinsic misalignment tolerance and lower sensitivity to coupling factor variation.
2. High coupling coefficient, due to their symmetric shape.
3. Scalability. The diameter of circular coils can be changed to make them bigger or smaller without significantly affecting system performance.
4. Straightforward fabrication, as they are easy to wind.
5. Readily available commercially. This would lower costs and production time if widespread adoption of this proposed WPT system occurs.

As explained in 3.1.3, coil modelling was carried out prior to physical winding of the coil in order to understand what an optimal number of windings would be. Various numbers of turns were simulated, with the wire being 0.1 x 350 Litz wire. The modelled characteristics are shown in Figure 15. Coils with 15 turns were selected due to their relatively high self-

inductance, while maintaining lower resistance. This is in contrast to the model, which might suggest that higher number of turns is better. In practice, the larger number of windings would result in a lower coil quality, and lower the power transfer.
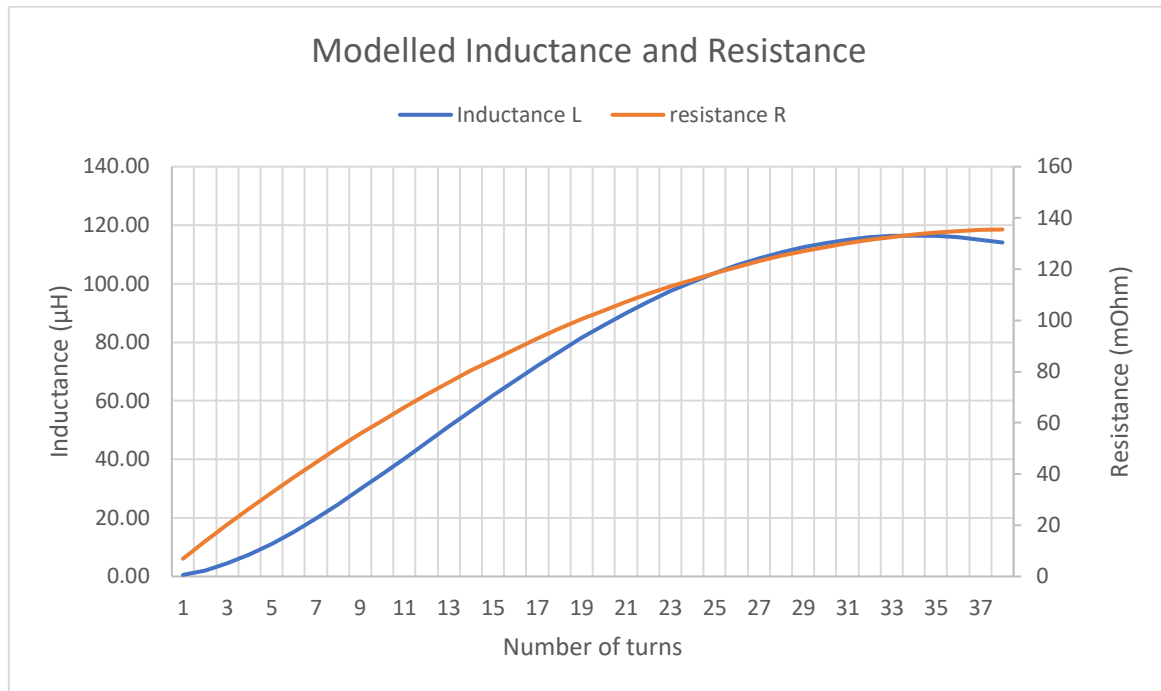

Figure 15: Coil modelling showing resistance and inductance for coils of outer diameter 230mm for varying number of turns.

I elected to use identical Tx and Rx coils for the highest coupling and power transfer efficiency. The Rx/Tx coils that were made are shown in figure 16, and the 230 mm outer diameter is shown in figure 17. As mentioned earlier, 0.1 x 350 Litz wire (350 strands of 0.1mm diameter each) was used. This is done to mitigate the 'skin effect', which is the increase of effective resistance to current at high frequencies [40]. It is caused by the current not penetrating fully into the conductor, and instead flowing more on the skin of the conductor.
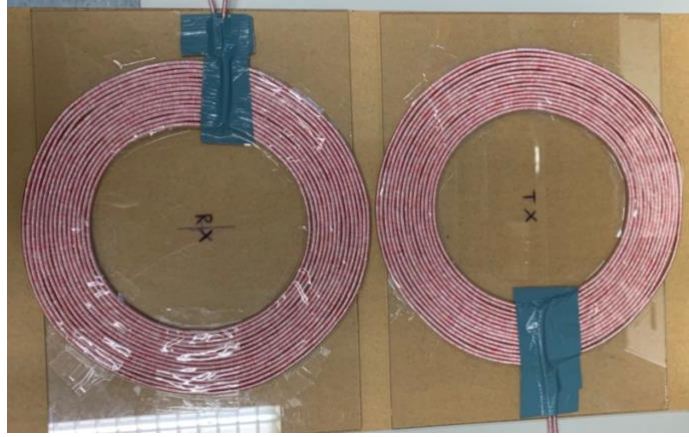
Figure 16: Identical Tx and Rx coils with 15 turns wound with Litz wire on acrylic glass.

Figure 17: Verification of 230 mm outer coil diameter.

3.2.4. *Determination of Operational Frequency:*

For a WPT system, the selection of the operational frequency is an important design decision that influences the system's performance and efficiency. However, since the operational frequency is interrelated with other aspects of the system, as shown in equation 12, it cannot be simply calculated, as there are more unknown variables than equations. Instead, it must be either determined experimentally, fixed arbitrarily, or calculated using another component value which has been arbitrarily fixed.

$$f_{res} = \frac{1}{2\pi\sqrt{LC}} \text{ , where } f_{res} \text{ and } C \text{ are both unknown} \qquad (12)$$

For the limited scope of this paper, I selected 100kHz as the operational frequency. This is justified as following:

1. Switching losses: Very high frequencies (several 100 kHz) can lead to increased switching losses in power electronic devices such as MOSFETs. At 100 kHz, a good balance between lower switching losses and efficiency may be achieved.

2. Compatible with existing systems: Many existing WPT systems reported in literature currently operate between 50 kHz and 300 kHz. This system can then be compared to them easily.

3. Lower skin effect: At 100 kHz the skin effect can be effectively mitigated by using Litz Wire, as the current will mostly penetrate throughout the 0.1 mm strands.

4. Convenience: Fixing the operational frequency allowed me to design the rest of the system effectively.

3.2.5. *Measurement of Inductances:*

I used two LCR meters: the Keysight E4980AL (Figure 18) and the Victor 4080 handheld meter (Figure 19) to measure the self-inductances and mutual inductance (M) for the coils respectively, using identical settings of 100kHz and 1V on each.

The method for deriving mutual inductance is from [41]. Initially, the device's input impedance is checked and series inductance L_X is measured with the primary and secondary coils connected as shown in Figure 20 (a). Next, this measurement is repeated again with the opposite series connection between the coils, as shown in in Figure 20 (b), giving us L_Y. The mutual inductance M is then calculated using:

$$M = \frac{L_X - L_Y}{4} \tag{11}$$

Figure 18: Keysight Technologies E4980AL Bench LCR Meter.
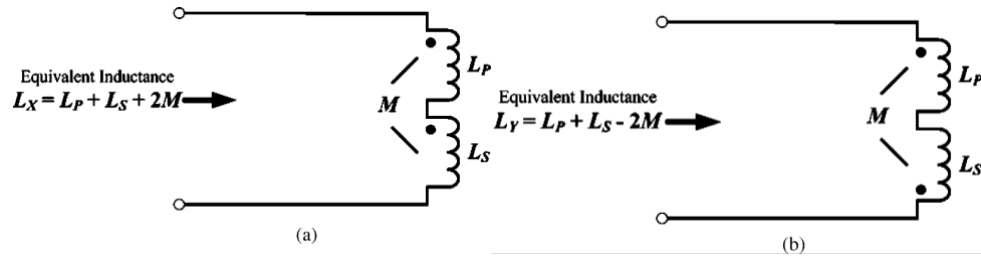
Figure 19: Victor 4080 handheld meter.

Figure 20: Different connections for mutual inductance measurement [41].
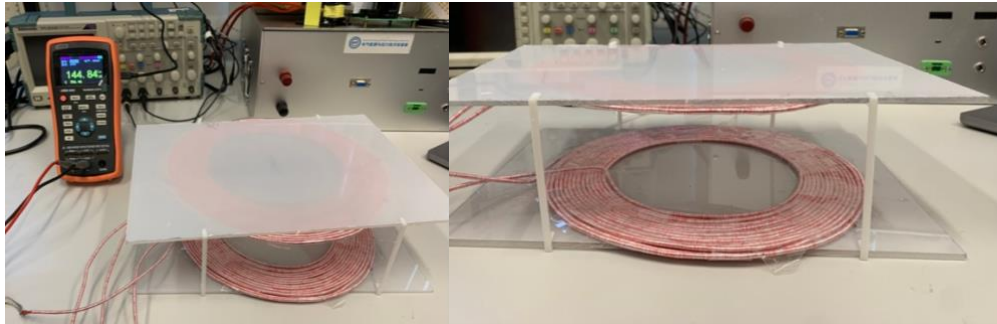
Figure 21: (a) Mutual inductance measurement, and (b) custom clips used for this.

The mutual inductance measurements were done across a varying set of heights. I designed and 3D printed sets of clips, seen in figure 21, that separated the Tx and Rx coils by a set distance. I tested distances between 0 cm and 10 cm as the Hunter SE rover has a ground clearance of 12.2 cm, seen in figure 14 (b), and certain margin has to be left for the electronics installation. Also, the calculation of coupling coefficient has been done here as well:

$$k = M\sqrt{Ls \cdot Lp} \tag{13}$$

Since the measurements are prone to error caused by interference from proximity to conductive materials, and the laboratory workbench is littered with these, the following steps were taken to mitigate errors:

1) For self-inductance measurements, each coil was lifted high above the workbench during measurement, to reduce the proximity to conductive materials.

2) The handheld meter was used on a separate desk for mutual inductance measurements as there was insufficient place on the workbench for the Rx/Tx coils to be placed without major interference with the readings.

3) Custom 3D printed clips were used to stabilise the coils and reduce error due to movement during mutual inductance measurement (Figure 21).

4) The average of two readings was taken for each measurement to reduce error.

The results for these measurements are shown in Table 1, Table 2, and figure 22.

Table 2: Self Inductance Measurements for Primary and Secondary Coil.

	Primary Coil Lp	Secondary Coil Ls	Unit
Series Inductance Ls	60.88	61.17	µH
Series Resistance Rs	84.30	85.00	mΩ

Table 3: Mutual Inductance Measurements for Coil System.

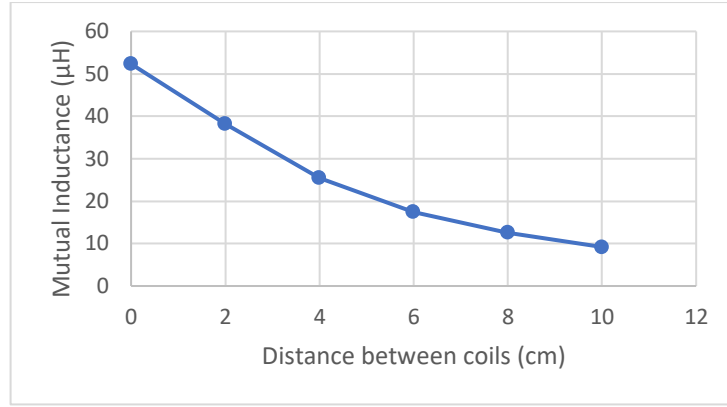| Spacer height (cm)	Lx (µH)	Ly (µH)	M (µH)	Coupling factor k
0	224.08	14.78	52.325	0.8574
2	193.35	40.46	38.223	0.6263
4	168.55	66.69	25.465	0.4173
6	154.16	84.21	17.488	0.2866
8	144.65	94.30	12.588	0.2063
10	137.83	101.06	9.193	0.1506

Figure 22: Mutual inductance vs coil separation.

3.2.6. *Selection of System Coil Separation:*

For the proposed WPT system designed for the Hunter SE rover, the maximum ground clearance of the robot is 12.2 cm. Also the mutual inductance has been tested for values between 0 cm and 10 cm. This concludes all the information needed for the selection of the separation distance for this system. A larger separation distance would have more margin for error and would be safer, as there would be lower chances of collision between the robot and the charging station. However, this would also result in lower coupling between the Rx and Tx coils, and thus lower efficiency of transfer. A lower separation would have higher coupling, but also greater chances of collision.

Thus, a moderately short separation distance of 4 cm is selected, which would allow high coupling with a low enough risk of collision.

3.2.7. *Simulation and Determining of LCC-S Compensation Values:*

I used MATLAB programs to calculate the inductor and capacitor values used in the LCC-S compensation network. The equations used are from derived from the basic equations for resonant circuits, as well as from [33]. For these calculations, the operational frequency of 100 kHz is entered. Also, to enable easy calculation, I fixed the value of the primary side series inductor to be 5 µH. This is also entered into the equations as a constant value. The MATLAB code used for the calculation is shown in figure 23. The results of the calculation are shown in figure 24.

The resulting values for resonance condition at 100 kHz are:

$L_{P1} = 5$ µH; $C_{P1} = 506.61$ nF; $C_{P2} = 45.33$ nF; $C_{S1} = 41.41$ nF

```
1    w=2*pi*100000;
2
3    Lt=60.88*10^(-6);
4    Lp1=5*10^(-6);|
5
6    Cp1=1/(w*w*Lp1);
7    Cp2=1/(w*w*Lt-w*w*Lp1);
8
```

```
1    w=2*pi*100000;
2    Lr=61.17*10^(-6);
3
4    Cs1=1/(w*w*Lr);
5
6
7
8
```

(a)   (b)

Figure 23: MATLAB calculations of LCC-S components. (a) Primary side. (b) Secondary side.

```
Workspace
Name ▲           Value
Cp1              5.0661e-07
Cp2              4.5330e-08
Cs1              4.1410e-08
Lp1              5.0000e-06
Lr               6.1170e-05
Lt               6.0880e-05
w                6.2832e+05
```

Figure 24: Calculated values of compensation network capacitors and inductor.

A spice simulation was also done to double check that the values have been calculated correctly. The simulation was set up to conduct an AC Analysis, and pass AC frequencies between 10k and 200k through the coils and compensation network. The output waveform was set to detect the voltage induced in the secondary coil, which should be highest at the resonant frequency of 100kHz if the system parameters are set correctly. Figure 25 shows the schematic for the simulation, figure 26 shows the result, which proves that the values were correctly calculated.
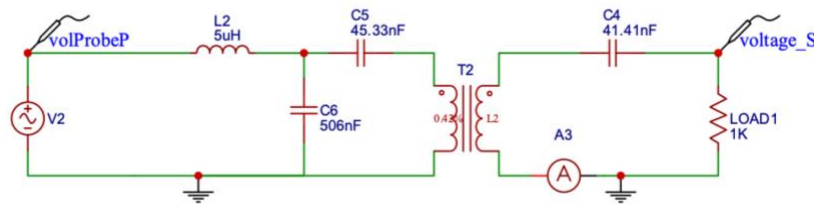

Figure 25: AC frequency analysis simulation in EasyEDA (uses the Ngspice engine).
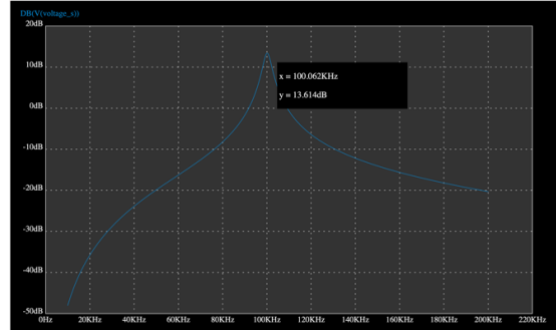
Figure 26: Simulation result, voltage in secondary coil highest at 100kHz frequency.

3.2.8. Custom Inductors and Capacitors:

Obtaining exact values for the capacitances and inductance involved in the LCC-S network is important for optimal performance of the WPT system. As seen in 3.2.6., the values are extremely specific, and thus cannot be readily purchased. For the capacitance values, several capacitors must combined in series and parallel to get the exact value. Non-polarized capacitors are used as the compensation network has to handle AC. Since the capacitors have error tolerances of ~1-5%, the values of each one had to be measured using the Victor 4080 handheld LCR meter prior to use (figure 27). After selecting all the smaller capacitors, I soldered them in parallel on proto-boards to obtain one large capacitor, as seen in figure 28. This was done for C_{P1}, C_{P2}, and C_{S1}.

For the inductor, while 5μH is not a difficult value to obtain readymade, it is better to hand-wind it. This allows the wire material and the inductance to be precisely controlled. Some benefits are:

1. Litz wire can be used: As explained in 3.2.3, the multi-stranded nature of Litz wire mitigates the skin effect. Since this inductor will compensate the WPT system at 100 kHz, this is necessary to increase the efficiency and keep effective resistance low.

2. Precise control: The inductor was hand-wound around an air core, which allowed for minute changes in the inductance to be realised. Around 6 turns were required to get close to 5μH. I then trimmed off small sections of wire and remeasured the inductance until an almost exact value of 5μH was achieved.

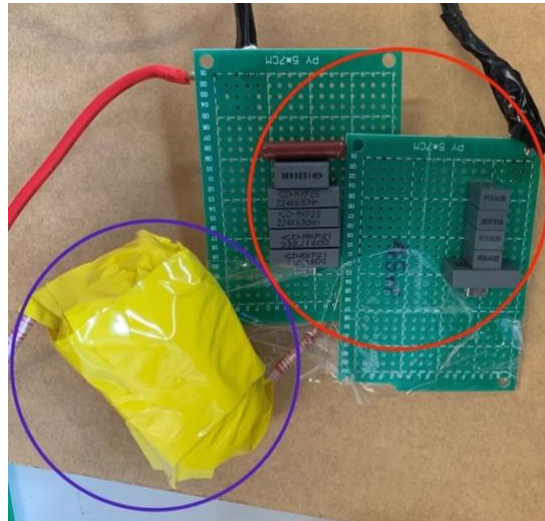Figure 27: Capacitance measurement using handheld LCR meter.

Figure 28: Hand-wound inductor Ls covered in Kapton tape (blue circle), Several parallel capacitors connected to form Cp1, Cp2. (red circle). The image shows all three components connected in LCC configuration.

3.2.9. *Selection of Microcontroller Board:*

The main consideration behind selection of these boards was 1) Speed and Processing Power: 32-bit microcontrollers, high clock speed, enough RAM and Flash memory, and 2) Ease of Development: I wanted to use Arduino compatible microcontrollers to leverage the large number of libraries available for the code.

For the control of the inverter, two microcontroller development boards were considered – PJRC's Teensy 4.1 and Texas Instruments LaunchXL-F28379D, both of which have 32-bit microcontroller units (MCUs). However, I chose the Teensy 4.1 board due to higher speed,

smaller form factor, ease of development, lower cost, and only needing a single core. Table 4 shows a comparison of the two board's features, and figure 24 shows the two boards side by side. For the IoT connectivity, ESP32 microcontroller boards, shown in figure 25, were selected. These are 32-bit MCUs with 2.4 GHz Wi-Fi and BT/Bluetooth LE support {Citation}. They are inexpensive, powerful, and are Arduino compatible. All the MCU boards are shown in figure 29.
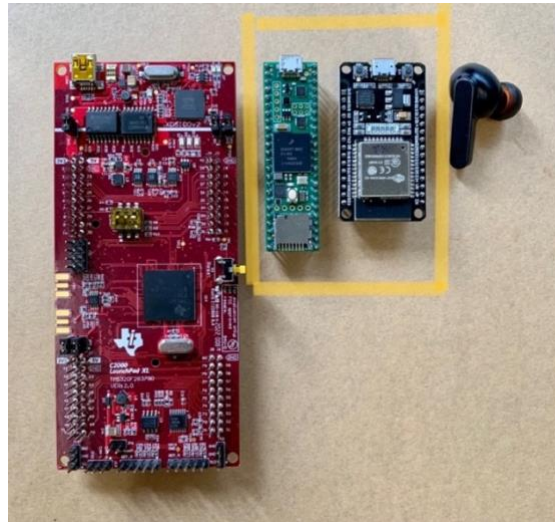

Figure 29: LaunchXL F28379D (far left), Teensy 4.1 (middle left), ESP32 (middle right), earbud for scale (far right). The highlighted boards are the ones being used.

Table 4: Comparison of Teensy 4.1 and LaunchXL 28379D [42], [43].

	Teensy 4.1	LaunchXL 28379D
Processor speed	600 MHz	200 MHz
Price	~ 32 USD	~ 58 USD
Memory	8Mbyte Flash, 1024KB RAM	512KB flash, 204KB RAM per core
Float math support	Yes	Yes
Cores	1	2
Arduino compatible	Yes	No

Chapter 4: Results

4.1.   Inverter Design:

To energise the Tx coil, two versions of the inverter were conceived. First, I designed a lower
power inverter (inverter A) to increase my familiarity with electronics design tools, and then
created the high power inverter (inverter B) that is finally used. Inverter A uses simpler
components that had extensive design guides available. The schematic for inverter A is
shown in figure 30. It uses bootstrapped high-side MOSFETs to provide them with sufficient
gate-drain voltage for switching. An advantage of this inverter is that it would allow the
frequency to be easily adjusted using a trim potentiometer connected to a NE555 timer IC.
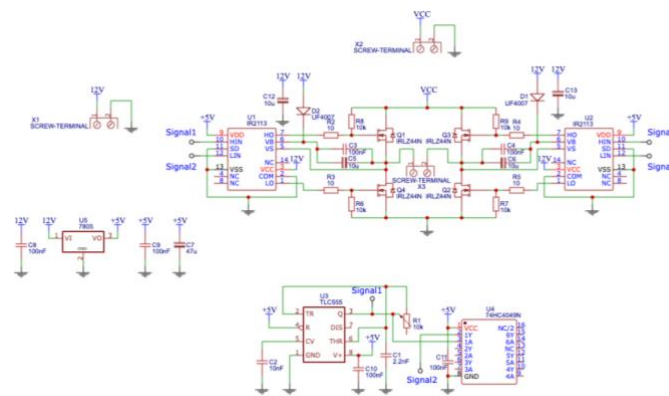

Figure 30: Lower power inverter A schematic.

However due to Inverter A's limitations in output power, maximum frequency, and control, I
designed Inverter B (schematic in figure 31). This is a high power, single phase, full H-bridge
inverter, capable of output of several hundred Watts. It also arranges the MOSFETs in a
bootstrap configuration. The two key components used are Woolfspeed C3M0060065K SiC
power MOSFETs, and Infineon 2EDF9275F gate driver ICs. These are meant for high power
and high speed switching. The fabricated, assembled inverter PCB is shown in figure 32.

An explanation of the working of this board is provided here: 4 Pulse-width modulation
(PWM) signals are used to control the four MOSFETs on the inverter. These are supplied to
four pin connector (H1). Three additional pins (H2) on the inverter PCB are used for
connection of voltage, ground, and enable/disable signal for the gate driver ICs. The screw
terminals on the board do the following: X1 is used to supply the high voltage (VCC) for the
output; X2 is used to supply the bootstrap gate drive voltage of 15V; X3 supplies the output

waveform, and is where the Tx coil would be connected. Many passive components (resistors, capacitors, diodes) are connected to enable this circuitry. An aluminium heatsink was also added to the MOSFETs on the inverter to enable prolonged high power use.
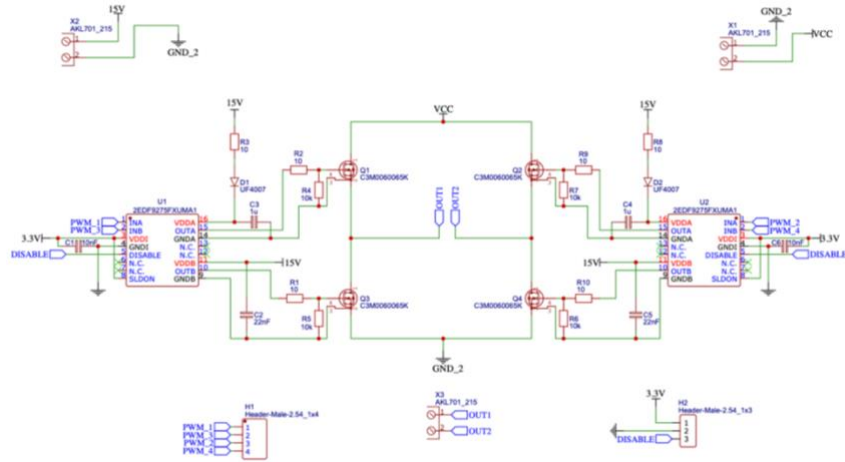

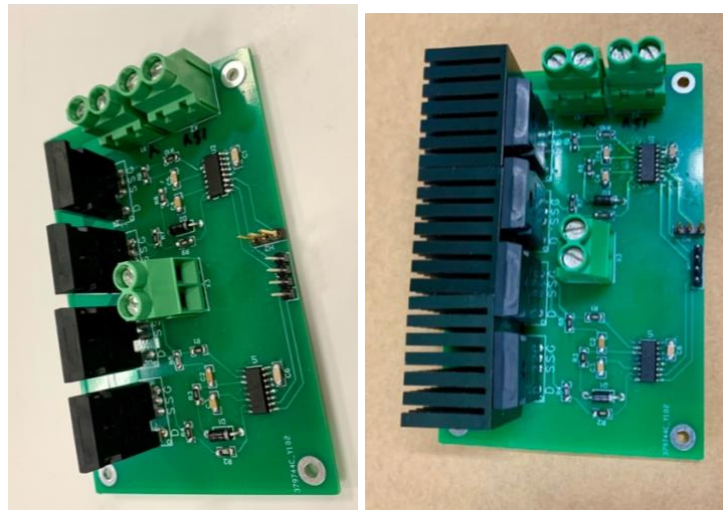Figure 31: Schematic of High Power Inverter (Inverter B).

Figure 32: Inverter B, before and after the addition of a heat sink

4.2. _Inverter Control:_

The primary side overall control board consists of the Teensy 4.1 and one ESP32 communicating with each other via the i2c protocol.

Figure 33 shows a section of the C++ code used in the Teensy 4.1 to control the inverter. The code for the inverter control makes use of the eFlexPWM module of the MX RT1062 MCU, as well as a library that facilitates easy and comprehensive use of all the PWM features that the board has to offer [44]. The PWM frequency is set to 100 kHz, and the duty cycle is fixed at 50%. The code activates 'complementary mode' for the PWM generation, which allows

the generation of two sets of complementary signals. Deadtime is also set, allowing each MOSFET enough time to close before the other one in the same half-bridge opens, to prevent current shoot-through . The phase shift is dynamically configurable, and the information for the degree of phase shift is received from the i2c connection to the ESP32. There is also a state machine set up with three modes. The Teensy receives information about the mode from the ESP32 via i2c. OFF mode disables the gate driver output, turning the inverter off. STANDBY mode enables the gate drive, increases phase shift to reduce output power, and pulses the Tx coil every 500ms. This is used to detect the presence of the Rx coil. ACTIVE mode generates the output PWM continuously for full inverter output, and allows for dynamic adjustment of phase shift. Figure 34 shows the inverter output in ACTIVE mode, with 90 degrees or 50% phase shift, which is standard operation. Figure 35 shows the inverter output during a pulse in STANDBY mode. The Tektronix TPS 2024B oscilloscope was used for visualisation of waveform results (figure 35).

```
void setup() {
  Serial.begin(9600);

  pinMode(DISABLE_PIN, OUTPUT);
  pinMode(LED_BUILTIN, OUTPUT);
  digitalWrite(DISABLE_PIN, LOW);     // Low = enabled

  Config myConfig;
  myConfig.setReloadLogic(kPWM_ReloadPwmFullCycle);
  myConfig.setPairOperation(kPWM_ComplementaryPwmA);
  myConfig.setPwmFreqHz(PwmFreq);
  // Initialize submodule
  Sm20.configure(myConfig);

  // Initialize submodule 2, make it use same counter clock as submodule 0.
  myConfig.setClockSource(kPWM_Submodule0Clock);
  myConfig.setPrescale(kPWM_Prescale_Divide_1);
  myConfig.setInitializationControl(kPWM_Initialize_MasterSync);

  Sm22.configure(myConfig);

  // Sm23.configure (myConfig);
  Tm2.setupDeadtime(100, 1000000000); // deadtime 100ns
  // synchronize registers and start all submodules
  Tm2.begin();

  Sm22.setupPwmPhaseShift(ChanA, phaseShiftPercent, true);
}
```
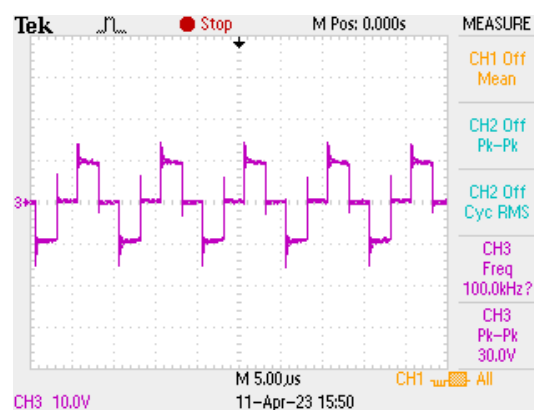
Figure 33: Section of inverter control code.

Figure 34: Inverter output with 50% phase shift.

Figure 35: Tektronix TPS 2024B Oscilloscope.

4.3. *Secondary and Primary Side Monitoring:*

For the secondary side, an ESP32 is used in conjunction with a DC current sensor module, as well as a DC voltage sensor module (shown in figure 36). These output analog signals, that are sampled by the analog-to-digital converter (ADC) of the ESP32. This allows measurement of the output voltage and current after the rectifier on the secondary side. This is used for two things: 1) Detection of Rx coil, and 2) Feedback for voltage output from inverter. The connections of the current and voltage sensor modules to the rectifier and the ESP32 is shown in figure 37. At the time of writing this report, the primary side sensing has not been implemented yet. However, the sensors for this have been identified, and integration should be complete by the final presentation. These are shown in figure 38.
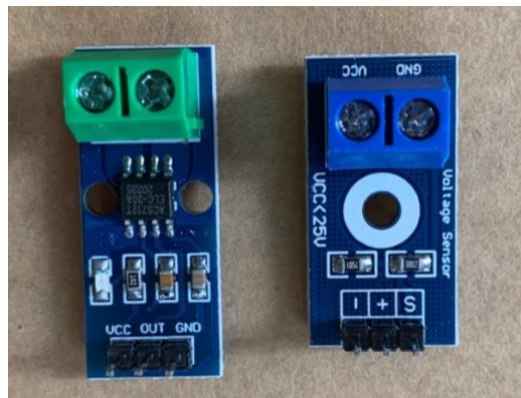

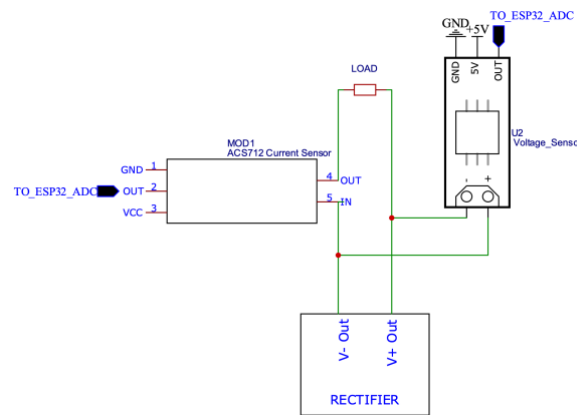Figure 36: (Left) Current sensor module, (right) voltage sensor module.

Figure 37: Connection of current/voltage sensor module to rectifier and ESP32.
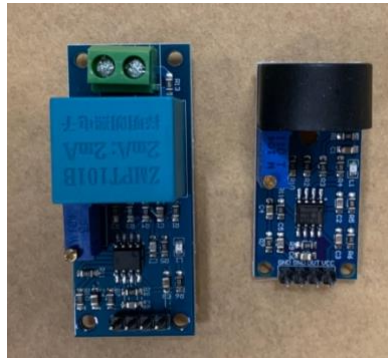
Figure 38: AC voltage sensor (left), AC current sensor (right). Both will be used on the Tx coil.

4.4. *Dashboard and Database:*

At the time of writing of this report, only a rudimentary dashboard has been created, which can show the voltage and current from the secondary side, as seen in Figure 39, as well as control the on/off state of the primary side. This was made using the Dart programming language and the Flutter framework. For the database, Firebase's Realtime Database was used, as seen in figure 40.

Figure 39: First version of the dashboard made with Flutter.

https://wpt-system-default-rtdb.asia-southeast1.firebasedatabase.app

https://wpt-system-default-rtdb.asia-southeast1.firebasedatabase.app/
alignment: "zero"
reciever
    current: 0
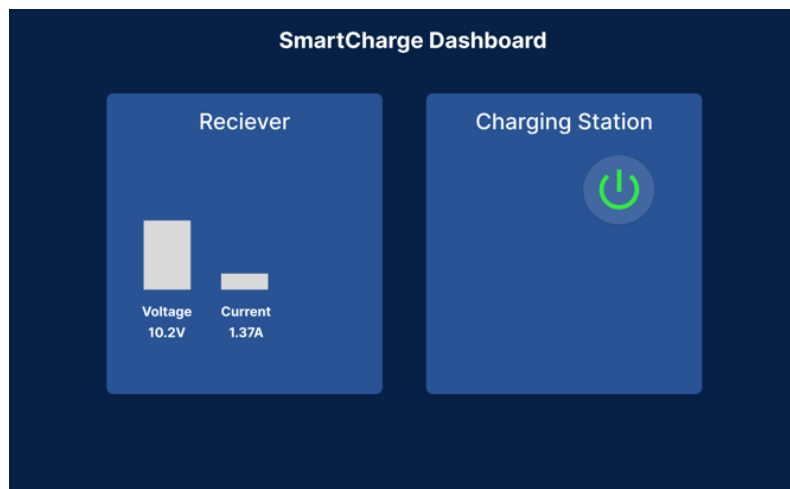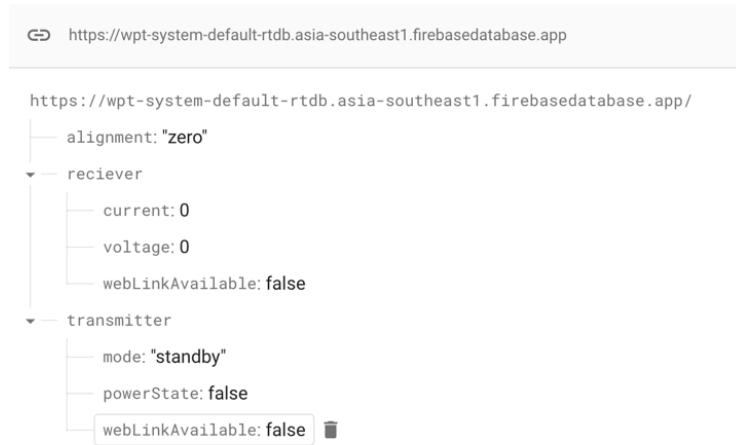   voltage: 0
    webLinkAvailable: false
transmitter
    mode: "standby"
    powerState: false
    webLinkAvailable: false

Figure 40: Schema of Firebase Realtime database used.

4.5. *WPT System Testing:*

Complete testing of the WTP system was done, and the efficiency of the system was tabulated. The system setup is shown in figure 41. ACTIVE mode operation, is seen in figure 42 (a) where voltage is successfully induced in the Rx coil, indicating power transfer. Also STANDBY mode, with its pulsing function was tested, and it works as expected. The waveform produced in this mode is shown in figure 42 (b). The extreme condition of phase-shift control was also tested and verified, where at 180 degrees phase shift, the waveform cancels out, and the lowest output voltage possible is produced (figure 43).
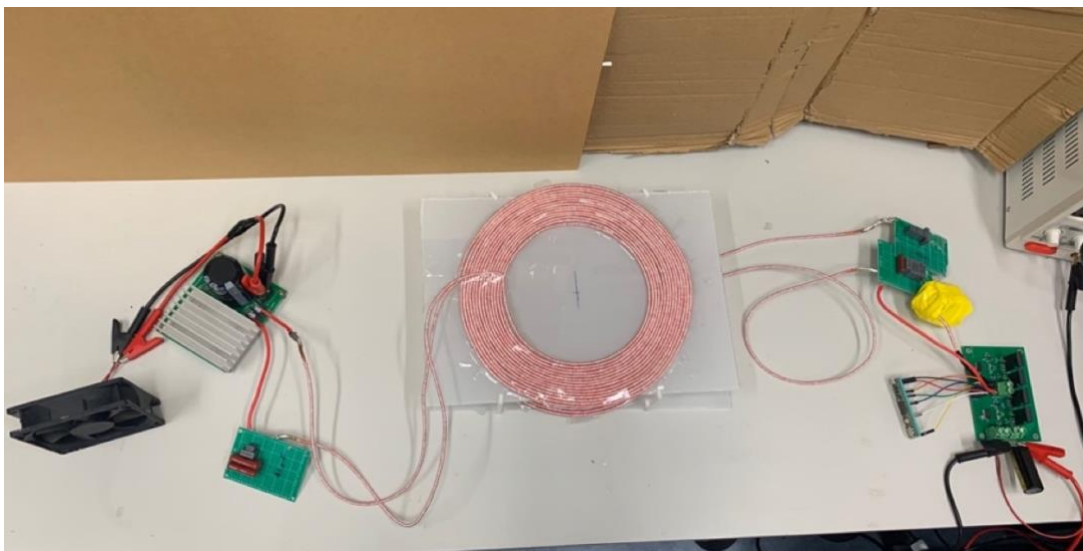

Figure 41: WPT system setup, with the primary side on the right, coils in the middle, and secondary side driving a 12V fan on the output.

(a)   (b)
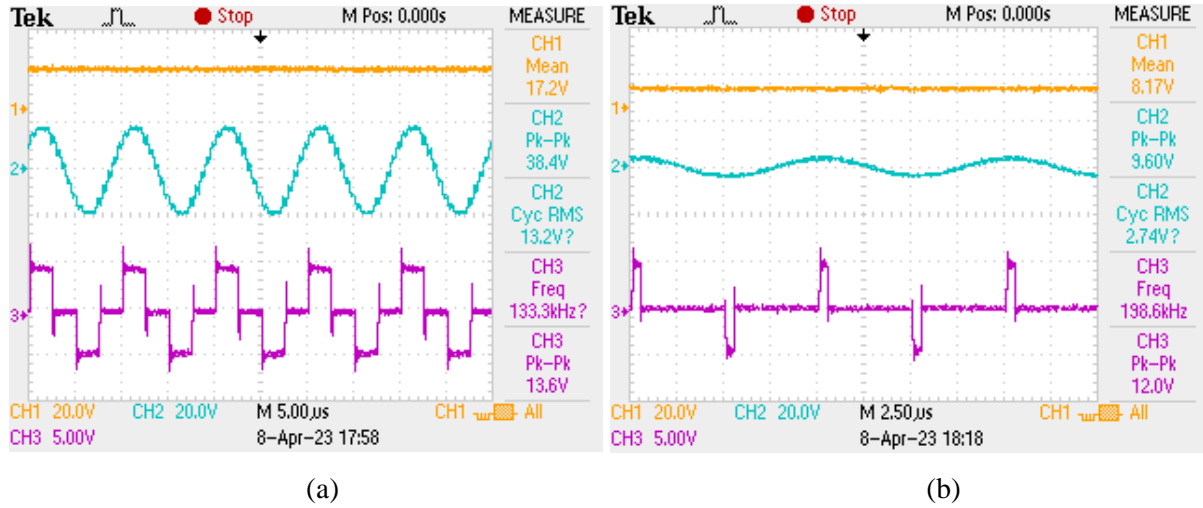
Figure 42: (a) Inverter output waveform during ACTIVE mode (purple), secondary induced voltage (blue), and output DC voltage (orange). (b) shows the same waveforms during STANDBY mode.
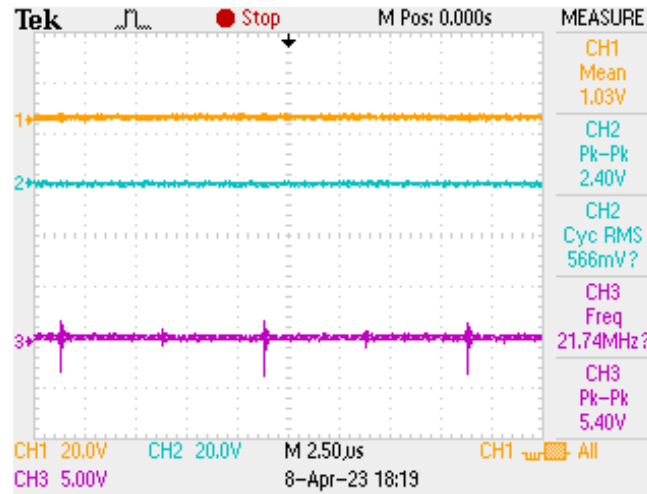
Figure 43: 180 degree phase shift output waveform. Minimum output power.

To test the efficiency of the system, the system was made to supply power to shunt resistors of known value. This allowed for the calculation of output power. Meanwhile, input power is known as it is shown by the DC power supply. The efficiency was then calculated as following:

$$\eta = \frac{P_{out}}{P_{in}} \tag{14}$$

The efficiency results are shown in table 5. It can be seen that a maximum efficiency of ~64 % was achieved, with a power transfer of 75.15 W. Higher voltage/current testing was not possible due to limitations of the lab bench power supply available.

Table 5: Efficiency results for WPT system under different load scenarios.

	V out (V)	I out (A)	P out (W)	Vin (V)	I in (A)	load (ohms)	P in (W)	efficiency (%)
5 V test	7.64	0.764	5.83696	5.04	2.31	10	11.6	50.14
10 V test	20.6	1.03	21.218	10	3.25	20	32.5	65.29
15 V test	36.3	0.726	26.3538	15	2.78	50	41.7	63.20
20 V test	48.9	0.978	47.8242	20	3.72	50	74.4	64.28
25 V test	61.3	1.226	75.1538	25	4.76	50	119	63.15

It should also be noted that when the Rx coil approached the Tx coil, the input waveform, and the induced voltage waveform were affected. This is due to the change in mutual inductance, and is a sign that the circuit is not properly compensated. This may occur due to small errors in the values of the capacitance and inductance used in the LCC network. This change in shape can be seen in figure 44.
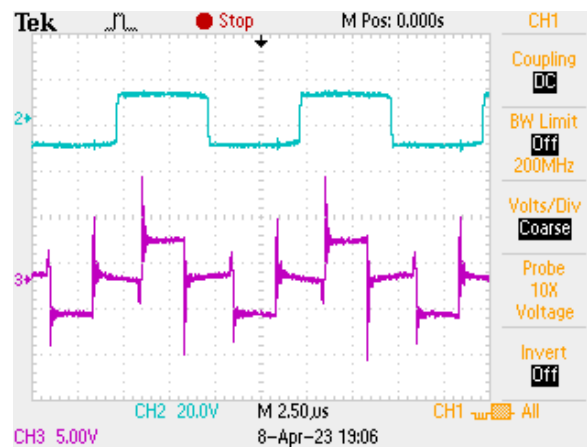

Figure 44: Change in shape of waveform under load. voltage induced in Rx (blue), and input waveform (purple).

Chapter 5: Recommendations for Future Work:

My recommendations for future studies in the area of smart WPT systems:

1. Generalisation of the system described in this paper, so that it can be applied to many more robots without significant modification to the parameters.

2. Explore the potential for scaling up the power transfer capacity of the system to accommodate larger and more power-intensive robotic applications, as this was not tested in the system in this paper.

3. Compare different IoT communication protocols (example: MQTT) to determine the most suitable option for various robotics WPT applications.

4. Investigate the implementation of a multi-device WPT system that can simultaneously charge several robots using the smart charging system.

5. Investigate the cybersecurity aspects of the IoT-integrated wireless charging system, as a lot of information is being transmitted to the cloud in this application.

6. Explore how machine learning or artificial intelligence techniques may be incorporated into the system for advanced monitoring and control capabilities, as well as for predicting the charging patterns of the robot.

Chapter 6: Conclusion:

In conclusion, this paper has successfully demonstrated the development and implementation of a smart wireless charging system for robotics, utilizing LCC-S compensation and integrating IoT technology for remote control, monitoring, and active feedback control. The system was designed for the Hunter SE rover shows high potential for integration with other robotic applications. With a maximum tested efficiency of 65% and a power transfer capability of 75 W over a 4 cm air gap, and higher power transfer possible based on the capabilities of the inverter, the smart wireless power transfer system stands out as a modern alternative to traditional wired charging solutions. The paper also successfully met the target of developing a truly smart WPT system that provides increased flexibility and convenience for users with the availability of information through the online dashboard.

Appendix:

Coil modelling extra information. These equations are used to calculate intermediate parameters W and R in the modelling of coil inductance in 3.1.3:

$$W\ (\text{width}) \ = \ \left(\frac{\text{wire diameter}}{25.4} \ + \ N \cdot \frac{\text{wire spacing}}{25.4} \right) \tag{15}$$

$$R\ (\text{radius}) \ = \ \frac{\left(\frac{\text{inner diameter}}{25.4} \ + \ W \right)}{2} \tag{16}$$

References:

[1] A. Marincic, "NIKOLA TESLA'S CONTRIBUTIONS TO RADIO DEVELOPMENTS," Heinrich Hertz Institute, Hamburg, Heinrich Hertz Institute, Hamburg, Oct. 2007, pp. 377–395. Accessed: Apr. 04, 2023. [Online]. Available: https://www.researchgate.net/publication/310801603_NIKOLA_TESLA%27S_CONTRIBUTIONS_TO_RADIO_DEVELOPMENTS

[2] A. Kurs, A. Karalis, R. Moffatt, J. D. Joannopoulos, P. Fisher, and M. Soljačić, "Wireless Power Transfer via Strongly Coupled Magnetic Resonances," *Science*, vol. 317, no. 5834, pp. 83–86, Jul. 2007, doi: 10.1126/science.1143254.

[3] A. Kurs, "Power transfer through strongly coupled resonances," Apr. 2009.

[4] A. Karalis, J. D. Joannopoulos, and M. Soljačić, "Efficient wireless non-radiative mid-range energy transfer," *Ann. Phys.*, vol. 323, no. 1, pp. 34–48, Jan. 2008, doi: 10.1016/j.aop.2007.04.017.

[5] M. Kesler, "Highly Resonant Wireless Power Transfer: Safe, Efficient, and over Distance," 2013.

[6] S. A. Mirbozorgi, H. Bahrami, M. Sawan, and B. Gosselin, "A Smart Multicoil Inductively Coupled Array for Wireless Power Transmission," *IEEE Trans. Ind. Electron.*, vol. 61, no. 11, pp. 6061–6070, Nov. 2014, doi: 10.1109/TIE.2014.2308138.

[7] S. Y. Hui, "Planar Wireless Charging Technology for Portable Electronic Products and Qi," *Proc. IEEE*, vol. 101, no. 6, pp. 1290–1301, Jun. 2013, doi: 10.1109/JPROC.2013.2246531.

[8] K. Li, U. Muncuk, M. Y. Naderi, and K. R. Chowdhury, "SoftCharge: Software Defined Multi-Device Wireless Charging Over Large Surfaces," *IEEE J. Emerg. Sel. Top. Circuits Syst.*, vol. 10, no. 1, pp. 38–51, Mar. 2020, doi: 10.1109/JETCAS.2020.2973814.

[9] N. Ha-Van, T. L. Vu, and M. Thuy Le, "An Efficient Wireless Power Transfer for Retinal Prosthesis using Artificial Intelligent Algorithm," in *2020 50th European Microwave Conference (EuMC)*, Jan. 2021, pp. 1115–1118. doi: 10.23919/EuMC48046.2021.9338235.

[10] Y. Liu, C. Liu, R. Huang, and Z. Song, "Primary Multi-frequency Constant-current Compensation for One-to-multiple Wireless Power Transfer," *IEEE Trans. Circuits Syst. II Express Briefs*, pp. 1–1, 2023, doi: 10.1109/TCSII.2023.3237078.

[11] X. Lu, D. Niyato, P. Wang, D. I. Kim, and Z. Han, "Wireless charger networking for mobile devices: fundamentals, standards, and applications," *IEEE Wirel. Commun.*, vol. 22, no. 2, pp. 126–135, Apr. 2015, doi: 10.1109/MWC.2015.7096295.

[12] Y. Zhou, C. Liu, and Y. Huang, "Wireless Power Transfer for Implanted Medical Application: A Review," *Energies*, vol. 13, no. 11, Art. no. 11, Jan. 2020, doi: 10.3390/en13112837.

[13] D. Patil, M. K. McDonough, J. M. Miller, B. Fahimi, and P. T. Balsara, "Wireless Power Transfer for Vehicular Applications: Overview and Challenges," *IEEE Trans. Transp. Electrification*, vol. 4, no. 1, pp. 3–37, Mar. 2018, doi: 10.1109/TTE.2017.2780627.

[14] S. Aldhaher, P. D. Mitcheson, J. M. Arteaga, G. Kkelis, and D. C. Yates, "Light-weight wireless power transfer for mid-air charging of drones," in *2017 11th European Conference on Antennas and Propagation (EUCAP)*, Mar. 2017, pp. 336–340. doi: 10.23919/EuCAP.2017.7928799.

[15] M. Tampubolon, L. Pamungkas, H.-J. Chiu, Y.-C. Liu, and Y.-C. Hsieh, "Dynamic Wireless Power Transfer for Logistic Robots," *Energies*, vol. 11, no. 3, Art. no. 3, Mar. 2018, doi: 10.3390/en11030527.

[16] W. C. Brown, "The History of Power Transmission by Radio Waves," *IEEE Trans. Microw. Theory Tech.*, vol. 32, no. 9, pp. 1230–1242, Sep. 1984, doi: 10.1109/TMTT.1984.1132833.

[17] W. Brown, "Experiments in the transportation of energy by microwave beam," in *1958 IRE International Convention Record*, Mar. 1964, pp. 8–17. doi: 10.1109/IRECON.1964.1147324.

[18] P. E. Glaser, "Power from the Sun: Its Future," *Science*, vol. 162, no. 3856, pp. 857–861, Nov. 1968, doi: 10.1126/science.162.3856.857.

[19] G. Mosca and P. A. Tipler, "27-4 Ampere's Law," in *Physics for Scientists and Engineers*, 5th ed.New York: W.H. Freeman, 2003, pp. 871–874.

[20] G. Mosca and P. A. Tipler, "28-2 Induced EMF and Faraday's Law," in *Physics for Scientists and Engineers*, 5th ed.New York: W.H. Freeman, 2003, pp. 899–902.

[21] J. Gubbi, R. Buyya, S. Marusic, and M. Palaniswami, "Internet of Things (IoT): A vision, architectural elements, and future directions," *Future Gener. Comput. Syst.*, vol. 29, no. 7, pp. 1645–1660, Sep. 2013, doi: 10.1016/j.future.2013.01.010.

[22] L. Atzori, A. Iera, and G. Morabito, "The Internet of Things: A survey," *Comput. Netw.*, vol. 54, no. 15, pp. 2787–2805, Oct. 2010, doi: 10.1016/j.comnet.2010.05.010.

[23] A. Azad, R. Tavakoli, U. Pratik, B. Varghese, C. Coopmans, and Z. Pantic, "A Smart Autonomous WPT System for Electric Wheelchair Applications With Free-Positioning Charging Feature," *IEEE J. Emerg. Sel. Top. Power Electron.*, vol. 8, no. 4, pp. 3516–3532, Dec. 2020, doi: 10.1109/JESTPE.2018.2884887.

[24] C. R. Teeneti *et al.*, "System-Level Approach to Designing a Smart Wireless Charging System for Power Wheelchairs," *IEEE Trans. Ind. Appl.*, vol. 57, no. 5, pp. 5128–5144, Sep. 2021, doi: 10.1109/TIA.2021.3093843.

[25] Y.-J. Kim, D. Ha, W. J. Chappell, and P. P. Irazoqui, "Selective Wireless Power Transfer for Smart Power Distribution in a Miniature-Sized Multiple-Receiver System," *IEEE Trans. Ind. Electron.*, vol. 63, no. 3, pp. 1853–1862, Mar. 2016, doi: 10.1109/TIE.2015.2493142.

[26] D. van Wageningen and T. Staring, "The Qi wireless power standard," in *Proceedings of 14th International Power Electronics and Motion Control Conference EPE-PEMC 2010*, Sep. 2010, pp. S15-25-S15-32. doi: 10.1109/EPEPEMC.2010.5606673.

[27] W. C. Cheah, S. A. Watson, and B. Lennox, "Limitations of wireless power transfer technologies for mobile robots," *Wirel. Power Transf.*, vol. 6, no. 2, pp. 175–189, Sep. 2019, doi: 10.1017/wpt.2019.8.

[28] M. Aboualalaa, H. Elsadek, R. K. Pokharel, M. Aboualalaa, H. Elsadek, and R. K. Pokharel, *WPT, Recent Techniques for Improving System Efficiency*. IntechOpen, 2021. doi: 10.5772/intechopen.96003.

[29] H. A. Wheeler, "Simple Inductance Formulas for Radio Coils," *Proc. Inst. Radio Eng.*, vol. 16, no. 10, pp. 1398–1400, Oct. 1928, doi: 10.1109/JRPROC.1928.221309.

[30] "Spiral Coil Calculator," *Kaizer Power Electronics*, Sep. 16, 2015. https://kaizerpowerelectronics.dk/calculators/spiral-coil-calculator/ (accessed Apr. 10, 2023).

[31] X. Qu, Y. Jing, H. Han, S.-C. Wong, and C. K. Tse, "Higher Order Compensation for Inductive-Power-Transfer Converters With Constant-Voltage or Constant-Current Output Combating Transformer Parameter Constraints," *IEEE Trans. Power Electron.*, vol. 32, no. 1, pp. 394–405, Jan. 2017, doi: 10.1109/TPEL.2016.2535376.

[32] Y. Chen, H. Zhang, C.-S. Shin, K.-H. Seo, S.-J. Park, and D.-H. Kim, "A Comparative Study of S-S and LCC-S Compensation Topology of Inductive Power Transfer Systems for EV Chargers," in *2019 IEEE 10th International Symposium on Power Electronics for Distributed Generation Systems (PEDG)*, Jun. 2019, pp. 99–104. doi: 10.1109/PEDG.2019.8807684.

[33] J. Yang, X. Zhang, K. Zhang, X. Cui, C. Jiao, and X. Yang, "Design of LCC-S Compensation Topology and Optimization of Misalignment Tolerance for Inductive Power Transfer," *IEEE Access*, vol. 8, pp. 191309–191318, 2020, doi: 10.1109/ACCESS.2020.3032563.

[34] M. Abou Houran, xu Yang, and W. Chen, "Magnetically Coupled Resonance WPT: Review of Compensation Topologies, Resonator Structures with Misalignment, and EMI Diagnostics," vol. 7, Nov. 2018, doi: 10.3390/electronics7110296.

[35] "Phase-Shifted Full Bridge DC/DC Power Converter Design Guide," 2014.

[36] "i.MX RT1060 Processor Reference Manual." [Online]. Available: https://www.pjrc.com/teensy/IMXRT1060RM_rev3.pdf

[37] "CyberDog Bionic Quadruped Robot," *Xiaomi*. https://www.mi.com/cyberdog/gallery (accessed Apr. 10, 2023).

[38] "HUNTER SE Rover," *Agilex Robotics*. https://global.agilex.ai/products/hunter-se (accessed Apr. 10, 2023).

[39] "Hunter SE." https://www.trossenrobotics.com/hunter-se.aspx (accessed Apr. 10, 2023).

[40] "XIII. On electrical motions in a spherical conductor," *Philos. Trans. R. Soc. Lond.*, vol. 174, pp. 519–549, Dec. 1883, doi: 10.1098/rstl.1883.0013.

[41] Y. P. Su, X. Liu, and S. Y. R. Hui, "Mutual Inductance Calculation of Movable Planar Coils on Parallel Surfaces," *IEEE Trans. Power Electron.*, vol. 24, no. 4, pp. 1115–1123, Apr. 2009, doi: 10.1109/TPEL.2008.2009757.

[42] "Teensy® 4.1." https://www.pjrc.com/store/teensy41.html (accessed Apr. 11, 2023).

[43] "LAUNCHXL-F28379D Development kit | TI.com." https://www.ti.com/tool/LAUNCHXL-F28379D (accessed Apr. 11, 2023).

[44] "eFlexPwm: eFlexPwm." https://epsilonrt.github.io/eFlexPwm/ (accessed Apr. 11, 2023).